JTTEE5 19:392–408
DOI: 10.1007/s11666-009-9383-5
1059-9630/$19.00 © ASM International

Peer Reviewed

Desirability-Based Multi-Criteria Optimization of HVOF Spray Experiments to Manufacture Fine Structured Wear-Resistant $75Cr_3C_2$-25(NiCr20) Coatings

W. Tillmann, E. Vogli, I. Baumann, G. Kopp, and C. Weihs

(Submitted April 24, 2009; in revised form July 10, 2009)

Thermal spraying of fine feedstock powders allow the deposition of cermet coatings with significantly improved characteristics and is currently of great interest in science and industry. However, due to the high surface to volume ratio and the low specific weight, fine particles are not only difficult to spray but also show a poor flowability in the feeding process. In order to process fine powders reliably and to preserve the fine structure of the feedstock material in the final coating morphology, the use of novel thermal spray equipment as well as a thorough selection and optimization of the process parameters are fundamentally required. In this study, HVOF spray experiments have been conducted to manufacture fine structured, wear-resistant cermet coatings using fine $75Cr_3C_2$-25(Ni20Cr) powders ($-8+2$ μm). Statistical design of experiments (DOE) has been utilized to identify the most relevant process parameters with their linear, quadratic and interaction effects using Plackett-Burman, Fractional-Factorial and Central Composite designs to model the deposition efficiency of the process and the majorly important coating properties: roughness, hardness and porosity. The concept of desirability functions and the desirability index have been applied to combine these response variables in order to find a process parameter combination that yields either optimum results for all responses, or at least the best possible compromise. Verification experiments in the so found optimum obtained very satisfying or even excellent results. The coatings featured an average microhardness of 1004 HV 0.1, a roughness Ra = 1.9 μm and a porosity of 1.7%. In addition, a high deposition efficiency of 71% could be obtained.

Keywords desirabilities, fine Cr_3C_2-NiCr powders (2-8 μm), HVOF, multi-criteria optimization, response surface models, statistical design of experiments (DOE)

1. Introduction

Thermal spraying has emerged as a suitable and effective surface engineering technology and is widely used to apply wear and corrosion protective coatings on various kinds of industrial applications such as tools, aero engine parts and valves, which are exposed to high mechanical load or intensive friction (Ref 1). Among the available thermal spray processes, the high velocity oxy-fuel spray (HVOF) technique is one of the most promising methods. Due to higher gas jet velocities and lower flame temperatures than many other thermal spray processes, HVOF spraying enables to produce sophisticated, wear-resistant cermet coatings with exceptional high quality regarding microstructure and surface finishing. These coatings generally feature a very low porosity, low oxidization and low carbide decomposition or carbide-matrix dissolution, resulting in high hardness and high abrasion resistance (Ref 2).

The reduction of the feedstock powder grain size to submicron or nanometric scale is of key interest in the thermal spray technology to develop novel fine structured or nanostructured cermet coatings with further enhanced structural and functional properties. Such coatings do not only show a significantly lower porosity than conventional coarse-structured coatings but also feature a higher surface quality. This enables the application of thin, near-net-shape coatings, for example, on forming tools which preserve the high shape and dimensional accuracy and meet highest demands regarding wear protection (Ref 3, 4). However, in contrast to conventional coarse-grained

This article is an invited paper selected from presentations at the 2009 International Thermal Spray Conference and has been expanded from the original presentation. It is simultaneously published in *Expanding Thermal Spray Performance to New Markets and Applications: Proceedings of the 2009 International Thermal Spray Conference*, Las Vegas, Nevada, USA, May 4-7, 2009, Basil R. Marple, Margaret M. Hyland, Yuk-Chiu Lau, Chang-Jiu Li, Rogerio S. Lima, and Ghislain Montavon, Ed., ASM International, Materials Park, OH, 2009.

W. Tillmann, E. Vogli, and **I. Baumann**, Faculty of Mechanical Engineering, Institute of Materials Engineering, Technische Universität Dortmund, Leonhard-Euler-Strasse 2, 44227 Dortmund, Germany; and **G. Kopp** and **C. Weihs**, Department of Statistics, Technische Universität Dortmund, Vogelpothsweg 87, 44227 Dortmund, Germany. Contact e-mails: wolfgang.tillmann@udo.edu, evelina.vogli@udo.edu, ingor.baumann@udo.edu, kopp@statistik.tu-dortmund.de, and weihs@statistik.tu-dortmund.de.

powders, the feeding and processing of fine particles <10 μm involves major difficulties. Due to the high surface to volume ratio and low specific weight, fine powders do not only provide a poor flowability in the feeding process, but also show a different thermo-kinetic behavior during spraying (Ref 5, 6). As a result of the high thermal susceptibility, fine powders tend to overheat rapidly in the spray process, leading to thermally induced phase transformations. Powder agglomeration, which might encounter in the feeding or thermal spraying process, represents another major problem. Agglomeration effects can lead to blockages in the powder feeder system, strong pulsations in the HVOF flame, or prevent the desired formation of a fine structured coating morphology during the spray process. In this case, the potentials provided by using fine powders would remain unused. Next to high thermal susceptibility, it has been observed that in contrast to coarse powders, fine particles are accelerated to higher velocities while passing the HVOF flame at equal parameter settings (Ref 7). This phenomenon can be explained by the fact that due to the lower specific weight fine particles are better captured and accelerated in the HVOF process gas flow. At the same time, fine particles show a significant tendency to lose their momentum and corresponding velocity when leaving the HVOF flame (Ref 7).

In thermal spray technology, Cr_3C_2-NiCr cermet coatings have been extensively used to mitigate abrasive and erosive wear at high temperatures up to 850 °C (Ref 8). However, next to the already mentioned problems encountered when processing fine particles, the use of fine Cr_3C_2-NiCr metal-matrix composite (MMC) powders with high metallic 25(Ni20Cr) content involves further difficulties. The strongly varying melting points of the metallic and carbide component can cause powder caking in the injectors and in the acceleration nozzle of the HVOF gun during spraying. Consequently, blockages might occur, which significantly decrease the deposition efficiency and eventually disrupt the thermal spray process. In order to process fine powders reliably, the use of appropriate process technologies and optimized parameters are fundamentally required (Ref 9). In this way, a particle overheating leading to powder caking can be reduced or even prevented. Furthermore, the fine structure of the feedstock powder can be preserved in the final as-sprayed coating morphology.

Other phenomena encountered in thermal spraying of fine Cr_3C_2-NiCr powder are the chemical degradation of the chromium carbides present in the feedstock powder or the reprecipitation and dissolution of the carbide phases into the NiCr matrix (Ref 10). These mechanisms are highly related to the size of the feedstock powder (Ref 11). The lower the powder grain size, the higher the thermal reactivity and consequently the higher the risk of decomposition effects or carbide-matrix reactions in the HVOF spray process. Crawmer et al. (Ref 12) and Russo and Dorfmann (Ref 13) explained the decarburization with the formation of Cr_7C_3 and $Cr_{23}C_6$ carbides in HVOF sprayed cermet coatings, which were detected using x-ray diffraction (XRD). However, Kreye et al. (Ref 14) pointed out that the presence of such phases in the as-sprayed coating morphology cannot be proven solely by the XRD approach, because their main diffraction peaks coincide with the lines referring to the NiCr and Cr_3C_2. Guilemany et al. and Matthews et al. also reported on the formation of CO and CO_2 in the HVOF flame while spraying with an excess of oxygen (Ref 8) and on a transformation of Cr_3C_2 to graphite during the spray process (Ref 15). Tao et al. (Ref 16) observed metastable Cr_2C phases in nanostructured Cr_3C_2-NiCr coatings deposited by means of HVAF technique. They attributed this effect to a rapid solidification of partly melted splats upon deposition. Matthews et al. (Ref 8) pointed out that these metastable phases might act as a large driving force for microstructural and compositional transformations when exposing such coatings to elevated temperatures. In addition, it is reported in their research work that the microstructure of the NiCr matrix phase in Cr_3C_2-NiCr coatings can vary with the spray conditions potentially ranging from zones of amorphous material to nano-crystalline and microcrystalline phases. As a result of these compositional decomposition effects, a variation and reduction of the hard carbide phase concentration in the coating morphology are obtained, leading to a decrease in hardness and wear resistance (Ref 8). Studies by Picas et al. showed that the coating microhardness obtained by HVOF spraying of fine powders with a grain size from 1.4 to 14.9 μm is significantly lower than the microhardness of coatings produced by using conventional powders (10-30 μm) of the same chemical composition (Ref 17). They related this effect to decarburization and decomposition of carbides during the HVOF process. It has been reported in research works by Li et al. that a rebounding of large Cr_3C_2 particles or agglomerates during the coating formation may also be another important reason for the carbon loss and the change of carbide content in the microstructure (Ref 17). Next to such effects, the formation of Cr_2O_3 oxides can occur on the outer surface of the Cr_3C_2-NiCr particles during spraying under atmospherical conditions or high HVOF process temperatures and may potentially be distributed within the body of the particles, if a widespread melting of the matrix occurs (Ref 18). The embedding of brittle oxide phases can negatively affect the morphology (e.g. by increasing the risk of cohesive breakages) and finally degrade the mechanical properties of the coating. Although modern HVOF systems allow reducing such thermally induced phase reactions and decomposition effects significantly through a sensitive thermal control of process gas flow, the use of fine Cr_3C_2-NiCr powders with high thermal reactivity still involves the mentioned difficulties above to a large extend. There is still a lack of knowledge about HVOF spraying of fine Cr_3C_2 carbides and it is yet unclear to what extent the final phase distribution and the coating crystallite sizes depend on the initial microstructure of the feedstock powder, particularly when submicron, nanosized or nanostructured cermet powders are used (Ref 19). Consequently, further research in the field of HVOF spraying of fine Cr_3C_2 carbides is necessary.

Statistical design of experiments (DOE) is known as an effective method for conducting a reduced number of

experiments in order to obtain optimized spray parameter settings to produce coatings with improved properties (Ref 20). In this study, statistical design of experiments (DOE) has been employed to identify the most relevant factors influencing the HVOF spraying of fine $75Cr_3C_2$-25(Ni20Cr) powders (−8 + 2 μm) and to find optimal settings for the deposition of fine structured cermet coatings with best mechanical and tribological properties. This has been accomplished in three design stages—Plackett-Burman, Fractional-Factorial and Central Composite designs—with the initial intention to consider all potentially important factors in very simple models (one for each response) in order to decide which variables to drop, and with the overall objective to build more sophisticated models for a few remaining, most relevant factors, which can be used for response surface modeling, i.e. prediction. As optima from different response surface models are usually contradictory, the concept of desirabilities (Ref 21) has been applied to combine all responses into one common measure—the desirability index, of which the optimum is directly associated with the optimum parameter settings.

2. Experimental

2.1 Powder Feedstock

Fine irregular and broken $75Cr_3C_2$-25(Ni20Cr) powders (Thermico SJA 660/48, −8 + 2 μm) were employed as feedstock material. A SEM picture of the powder morphology and the grain size distribution analyzed by laser diffractometry (Microtrac, USA) is illustrated in Fig. 1. In order to minimize agglomeration effects, the fine powder was heated up to 120 °C in a convection oven for 1 h before use in the feeder system.

2.2 Substrates

Rectangular (70 × 50 × 10 mm) C45 steel specimens (1.0503) were employed as substrate material. In preparation for thermal spray experiments, the surfaces were grit-blasted with fine-grained F100 alumina (grain size: 106-150 μm) using a blasting air pressure of 3 bar, a stand-off distance of 100 mm and a blasting angle of approximately 45°. After the blasting procedure, the C45 substrate surface showed an average roughness of Ra = 1.42 ± 0.11 μm. Subsequently, the samples were cleaned for 15 min in an ethanol ultrasonic bath and heated to 110 °C in a convection oven for about 30 min.

2.3 Coating Process

A Thermico CPF2-Twin powder feeder system equipped with two vibratory powder containers, which is optimized for the reliable processing of fine powder fractions, was used to feed the fine particles into the HVOF gun. In order to minimize the risk of particle agglomerations, both powder containers were heated up to 60 °C with heating sleeves and were agitated with a pneumatic vibrator at a pressure of 6.2 bar. In addition, a cyclical evacuation of the two powder containers and a subsequent hot powder gas flushing at 80 °C were performed prior to the feeding operation. A Thermico CJS-HVOF gun with novel K5.2 combustion chamber design and dual-radial powder injection was used to conduct the coating experiments. This HVOF system operates with a two-stage hydrogen-oxygen and a subsequent liquid fuel (kerosene) oxygen combustion (Ref 22), which allows to control the velocity and the temperature of the process gas flow almost independently (Ref 7). For the coating experiments, EXXSOL D 60 kerosene (ExxonMobil Chemical Central Europe GmbH, Germany) was used as a liquid fuel. During the coating experiments, the backsides of the specimens were constantly cooled with compressed air.

2.4 Statistical Design of Experiments

For the coating experiments, the HVOF gas composition consisting of the kerosene (KL), hydrogen (HL) and oxygen (OL) levels as well as the gun velocity (GV), the stand-off distance (SOD), the specimen's backside compressed-air cooling pressure (BCP), the carrier gas level (CGL) and the feeder disc velocity (FDV) were selected as independent factors. All powder feeder

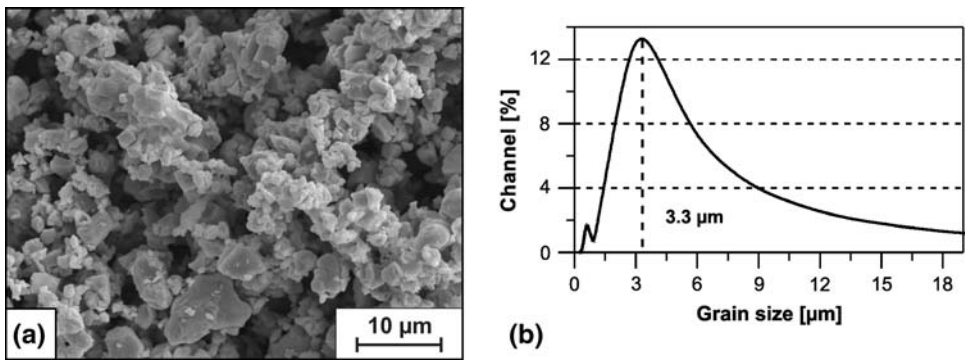

Fig. 1 (a) Structure of the fine $75Cr_3C_2$-25(Ni20Cr) powders taken by SEM; (b) powder grain size distribution analysis

settings (the feeder disc velocity and the carrier gas level) were applied to each of both powder containers. Pilot tests were initially carried out to find two expedient level settings (low and high) for each variable. These level settings were converted to −1 (low) and +1 (high) for the DOE. In the pilot tests, the powder injected HVOF jet was directed perpendicularly onto planar steel samples. Different spray process parameters (kerosene-, oxygen- and hydrogen level, stand-off distance) and powder feeding parameters (feeder disc velocity, carrier gas level) were varied and tested to produce a focused coating material spot showing a suitable melting behavior of the MMC feedstock material with an unimodal profile. Whereas one parameter was varied, the other ones were kept constant (one-factor at a time variation) in order to find suitable process parameter settings for the DOE. In a screening step, all factors were subjected to a 12-run Plackett-Burman design and their effects on the deposition efficiency (DE) and the coating characteristics microhardness (MH), porosity (Po) and roughness (RRa) were estimated in four separate linear models. Afterwards, the effects of the five most relevant factors were analyzed along with all possible two-way interaction effects in a 2^{5-1} fractional-factorial design with 16 runs. Three additional center runs (level 0) were carried out to enable the estimation of the overall variance. Finally, the factors KL, OL and SOD were arranged in a Central Composite design. In all designs, the run order of experiments was randomized to avoid a systematic bias. Using response surface models based on the Central Composite design and the concept of desirabilities (Ref 21), an overall optimum process parameter setting was determined in a multi-criteria optimization approach. All analyses were carried out with the free statistics software "R" (Ref 23) and Statistica v7 [StatSoft (Europe) GmbH, Germany].

2.5 In-Flight Particle Diagnostics and Coating Characterization

The temperature and the velocity of the HVOF sprayed particles were measured in-flight with an Accuraspray-g3 device (Tecnar, Canada). Characterizations of the coatings in terms of hardness, porosity and roughness were performed. The surface roughness was measured according to the DIN 4760 standard with a T-1000 tracing stylus instrument (Hommel, Germany). A M-400 microhardness tester (LECO, Germany) was employed to ascertain the coating microhardness. Cross-sectional images of the coatings were taken by an AXIOPHOT light microscope (Zeiss, Germany) and the layer thickness was determined. The porosity was analyzed with the integrated image analysis software Axiovision 4.63 Outmess at a magnification level of 200, degressive contrast amplification (using gamma-function) and medium illumination level. Cross-sectional images of the coating with higher magnification were made using a JXA 840 scanning electron microscope and a Jeol JSM-7001F field emission scanning electron microscope with both secondary-electron and backscattered electron detectors (Jeol, Germany). Element analyses of the coating structure were carried out using the integrated energy dispersive x-ray (EDX) device INCA x-act (Oxford Instruments, Germany). In addition, the deposition efficiency was determined. The wear and friction behavior of the fine structured $75Cr_3C_2$-25(Ni20Cr) were analyzed with a Pin-on-Disc tribometer tester (CSM, Switzerland) using an alumina ball (Ø 6 mm) with a hardness of 1986 HV 0.1. For this purpose, four different tracks with diameters of 18, 24, 30 and 36 mm were made on the coating surface. The analyses were carried out at a track velocity of 0.4 m/s, a wear distance of 250 m and a load of 10 N without lubrication and at ambient temperature. Besides the Pin-on-Disc test a Taber Abraser (Taber Industries, Model 505 Dual Abrasion Tester) was additionally employed to determine the wear coefficient of the coatings. For this purpose, Calibrade H-10 (medium coarse) abrading wheels composed of a non-resilient, vitrified binder and aluminum oxide/silicon carbide abrasive particles, a load of 2 × 1 kg, a wear distance of 1000 m and a track velocity of 14 m/min have been utilized. Prior to both tribologic examinations, the coated Pin-on-Disc and Taber Abraser samples were face grinded to a roughness of Rz < 1 μm using a 54 μm diamond-Bakelite abrasive disc. This procedure is necessary to provide a defined and continuous contact between the ball and the substrate's surface. In addition, Pin-on-Disc tests have also been performed with as-sprayed (not grinded) coatings. The adhesive strength was determined according to the DIN EN 582 standard using a mono-axial tensile test device type UPD 10 (Mohr and Federhaff AG, Germany) with a maximum capacity of 100 kN and a single-pack epoxy resin adhesive, ULTRA BOND 100 (HTK Hamburg GmbH, Germany).

3. Pilot-Tests and Experimental Designs

3.1 Pilot-Tests for the Parameter Level Identification

The pilot tests showed that the formation of powder caking in the powder injectors and in the acceleration nozzle represented the most significant problem while processing of fine $75Cr_3C_2$-25(Ni20Cr) composite powders. This effect occurred mainly at high kerosene levels ≥11 L/h and is also supported by insufficient carrier gas flows <9 L/min or >11 L/min. Figure 2(a) illustrates the powder caking inside the acceleration nozzle of the CJS-HVOF system after thermal spraying of approximately 15 min in comparison to an unused one (Fig. 2b). It is also demonstrated in Fig. 2(b) that spraying with optimized parameters (kerosene level <11 L/h and carrier gas flows between 9 and 11 L/min) significantly helps to reduce such powder caking inside the acceleration nozzle. High kerosene levels lead to an increased heat density in the HVOF process gas flow and to an intensified post-combustion in the free jet. Consequently, an increase in the thermal energy of the HVOF process and in the particle temperature is observed. It is assumed that on entering the hot HVOF process gas flow, different degrees of fusion and

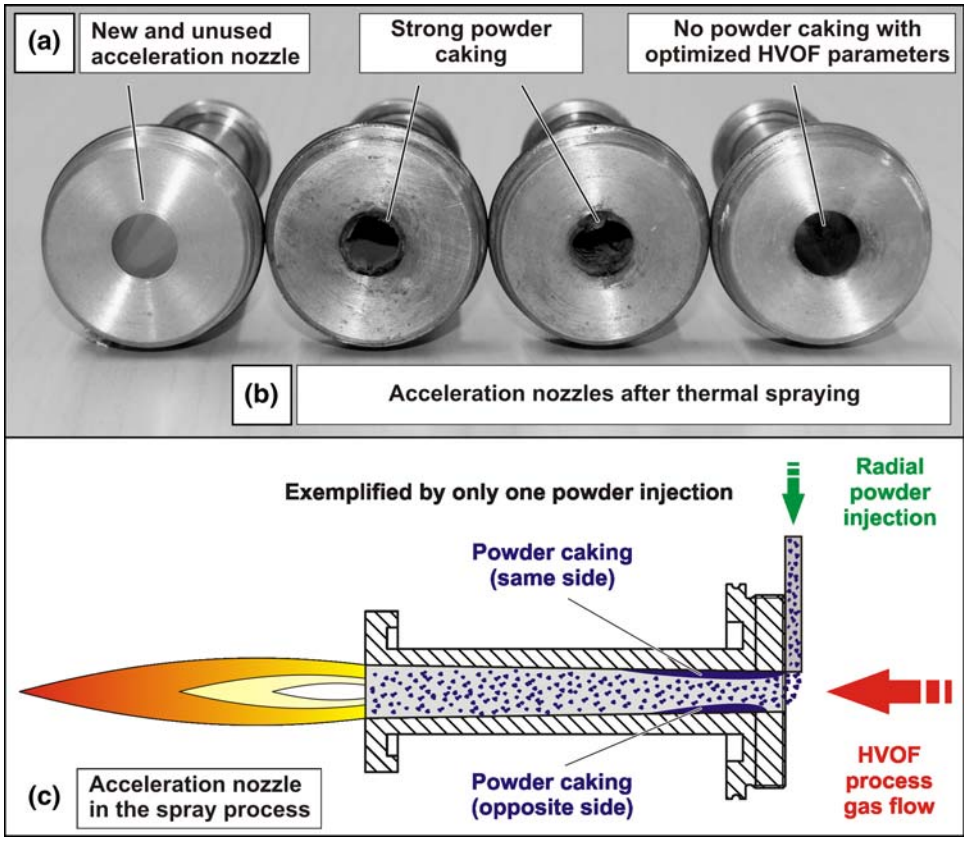

Fig. 2 Powder caking formation inside the HVOF acceleration nozzle

kinetic injection behaviors of metallic nickel chromium and chromium carbide particles, majorly depending on the grain sizes are obtained (Ref 19, 24). Another important factor is the lower melting point of the metallic 25(Ni20Cr) component leading to a premature melting compared with the chromium carbides at high HVOF gas temperatures and low flame velocities.

During the injection in the HVOF process gas flow at high kerosene level ≥11 L/h, the fine $75Cr_3C_2$-25(Ni20Cr) particles show a high tendency to impact either at the opposite inner side of the acceleration nozzle or at the side where the powder leaves the powder injector (Fig. 2c), leading to a powder caking formation. At high argon carrier gas flows >11 L/min, the powder is accelerated to higher velocities and is able to pass through the supersonic HVOF process gas flow. Consequently, the molten particles impact predominantly at the opposite inner side of the acceleration nozzle. However, at carrier gas flows <9 L/min, a contrary effect is achieved. Due to the fact that the powder is injected dual radially at opposite sides in the acceleration nozzle (the two powder injectors are radially positioned at an angle of 180°), the use of insufficient carrier gas flows <9 L/min or >11 L/min at high kerosene levels ≥11 L/h led to the formation of powder caking at both inner sides of the acceleration nozzle in all experiments.

It could also be observed that during spraying with high kerosene levels ≥11 L/h in combination with short stand-off distances of 100 mm agglomerates which are formed by powder caking are periodically peeled-off the acceleration nozzle and are able to embed in the coating morphology, as shown in Fig. 3(a). These agglomerations do not only result in high surface roughness but also disrupt the functional abilities of the coating with respect to wear protection and the superior surface finishing which should particularly be provided by fine structured coatings without any additional grinding processes. Two possible reasons seem to be evident to explain this phenomenon. On the one hand, the formation of such powder agglomerations may already occur during the feeding process as a result of the high surface to volume ratio. However, due to the fact that varying powder feeding parameters in selected and sufficient intervals (feeder disc velocities between 2.0 and 2.6 rpm and carrier gas flows between 9 and 11 L/min) do not show a major influence on this effect, it is more likely that these agglomerations are formed during the spraying process, particularly when the powders enter the hot supersonic HVOF process gas flow through the powder injectors in the acceleration nozzle.

These agglomerations show a periodical, recurring structure in the coating morphology, comparable to a texture. Therefore, it is assumed that this phenomenon can be attributed to a periodical formation and delaminating of powder caking in the powder injectors and the acceleration nozzle, particularly occurring at high

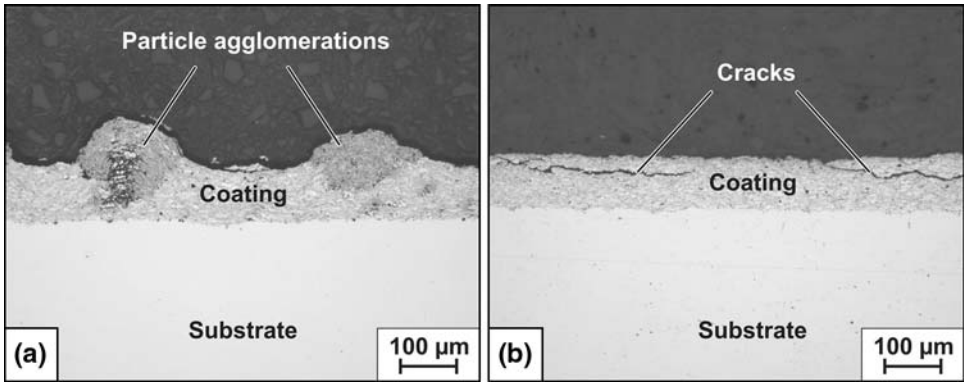

Fig. 3 (a) Powder agglomerations and (b) cracks in the coating morphology

kerosene levels ≥11 L/h. After being peeled off from the injectors and the acceleration nozzle by the supersonic HVOF process gas flow, the agglomerate is heated up. Due to the large size and the higher mass of the agglomerates than the fine (non-agglomerated) spray particles at high kerosene levels, a predominant melting of the surface regions of the agglomerates is obtained while the cores remain mostly solid. This effect is supported by shorter stand-off distances (100 mm). Because of this short stand-off distance, a shorter dwell and heating time of the agglomerated powder particles, passing the HVOF gas flame, is obtained, which prevents a continuous and sufficient melting of the core. Consequently, the combination of high kerosene flows ≥11 L/h and short stand-off distances of 100 mm should be avoided to minimize the risk of powder agglomerations and their embedding in the coatings.

Significantly higher kerosene levels of 16 to 18 L/h caused the formation of considerable and unacceptable powder caking in the powder injectors and in the acceleration nozzle which led to a strong decrease in the deposition efficiency during spraying and eventually to a disruption of the HVOF process. Additionally, it has been shown that independent from all other coating parameters, short stand-off distances of 100 mm also support the formation of horizontal cracks in the coatings microstructure, leading to cohesive breakages or delaminations between the coating lamellae (Fig. 3b).

This effect can be explained by two interdependent reasons. On the one hand, a short dwell time of the powder particles passing the HVOF process gas flow at short stand-off distances of 100 mm leads to an insufficient particle heating and melting. Due to the fact that many of the sprayed particles, which impact the substrate surface, are in an almost solidified state, only a poor embedding in the coating morphology is achieved. This leads to a reduced cohesion strength between the individual coating lamellae and increases the risk of a crack formation. On the other hand, this effect is particularly supported by a thermal stress development in the coating structure during spraying at short stand-off distances of 100 mm, because a major part of the HVOF flame strikes the surface and transfers a high amount of thermal energy to the substrate surface. The continuous and periodic passing of the HVOF gun over the surface of the substrate at short stand-off distances of 100 mm causes a strong thermal cycling. The corresponding temperature gradient leads to the development of thermally induced stress and to a crack formation.

In addition, higher feeder disc velocities ≥3 rpm were associated with increasing risks of blockages in the feeding hose and also led to an oversaturation of the HVOF flame. Consequently, not all particles in the HVOF flame could reach a molten state anymore and bounced off after hitting the substrate surface, leading to a significant decrease in deposition efficiency. Therefore, feeder disc velocities ≥3 rpm were not used in further experiments.

3.2 Placket-Burman Design (Screening)

Table 1 summarizes all factor levels which have been used and varied in the three consecutive design stages (Plackett-Burman, Fractional-Factorial and Central Composite design). With the intention to reduce the number of factors and to concentrate on the remaining, majorly important ones in the subsequent designs a 12-run Plackett-Burman design (Ref 25) was initially carried out at two factor levels (+1 and −1) as a screening of possibly important process parameters.

Under the assumption of a multiple linear model for each response variable Y (Eq 1) with normally distributed errors $\varepsilon \sim N(0, \sigma^2)$,

$$Y = \beta_0 + \beta_1 x_1 + \cdots + \beta_p x_p + \varepsilon \quad \text{(Eq 1)}$$

an overall mean β_0 (intercept) and main effects β_i of $p = 8$ influence factors were estimated. Significance tests of the null hypothesis H_0 of no effect of each of the independent variables x_i on the respective Y (i.e. $\beta_i = 0$, $i = 1, \ldots, 8$) were performed at a significance level $\alpha = 0.2$ to help decide upon the most important influence factors. The corresponding p-values, providing an intuitive measure of the probability mass in favor of the null hypothesis, are presented in Table 2. p-Values below the chosen alpha give little support for the null hypothesis and lead to a rejection of H_0. The associated factor x_i is then assumed to affect the respective Y positively or negatively, depending on the

Table 1 Factor levels in the three design stages

	Plackett-Burman design		Fractional-Factorial design			Central Composite design				
Factor	**-1**	**+1**	**−1**	**0**	**+1**	**−2**	**−1**	**0**	**+1**	**+2**
Kerosene level (KL), L/h	7	9	8	9	10	8	9	10	11	12
Hydrogen level (HL), L/min	60	80	60	80	100			80		
Oxygen level (OL), L/min	800	900	800	850	900	750	800	850	900	950
Gun velocity (GV), mm/min	20000	30000		30000				30000		
Stand-off distance (SOD), mm	120	140	100	130	160	100	115	130	145	160
Backside cooling pressure (BCP), psi	20	60		20				20		
Carrier gas level (CGL), L/min	9	11		11				11		
Feeder disc velocity (FDV), rpm	2.0	2.6	2.3	2.6	2.9			2.6		

Table 2 Effect estimates and *p*-values (α = 0.2) for the Plackett-Burman design

	Microhardness (MH), HV 0.1		Roughness Ra (RRa), µm		Porosity (Po), %		Deposition efficiency (DE), %	
	Estimate	***p*-Value**	**Estimate**	***p*-Value**	**Estimate**	***p*-Value**	**Estimate**	***p*-Value**
Intercept	578.7	NA	3.65	0.0000	1.24	0.0074	24.92	0.0003
Kerosene level (KL)	127.0	NA	−0.76	0.0001	−0.77	0.0272	2.61	0.1249
Hydrogen level (HL)	25.3	NA	−0.21	0.0069	−0.17	0.4448	1.18	0.4086
Oxygen level (OL)	9.3	NA	0.43	0.0008	−0.25	0.2797	0.99	0.4827
Gun velocity (GV)	−27.8	NA	−0.03	0.4144	0.25	0.2797	4.01	0.0477
Stand-off distance (SOD)	−22.0	NA	−0.14	0.0204	0.30	0.2067	−2.08	0.1905
Backside cooling pressure (BCP)	−24.5	NA	0.01	0.8237	0.21	0.3464	−0.71	0.6047
Carrier gas level (CGL)	13.3	NA	−0.13	0.0257	−0.13	0.5333	−0.77	0.5793
Feeder disc velocity (FDV)	16.7	NA	−0.03	0.4640	0.08	0.7020	1.49	0.3155

sign of the estimate. The *p*-values are calculated on grounds of a *t*-distribution with *n-p*-1 degrees of freedom of the *t*-statistic according to Eq 2 where β_i is the estimate of β_i and $s_{\hat{\beta}_i}$ is the estimate of the standard error of $\hat{\beta}_i$.

$$t = \frac{\hat{\beta}_i - 0}{s_{\hat{\beta}_i}} \qquad \text{(Eq 2)}$$

Based on the results in Table 2, KL was identified as the most important factor, but also HL, OL and SOD showed strong significances, in particular with respect to RRa. Due to the slight but positive influence of GV on DE, GV was held constant at the highest possible setting 30000 mm/min in further experiments. Similarly, CGL was fixed at the highest reasonable level of 11 L/min as the high level of CGL was associated with less roughness of the surface. As explained in the section about pilot tests, higher CGL settings than 11 L/min are not suitable due to the increasing risk of a powder caking formation inside the powder injectors and the acceleration nozzle of the HVOF gun. BCP showed no significant results and was further held constant at 20 psi, because this setting seems to be sufficient to avoid an overheating of the substrates surface during the spray process and only leads to a low affection of the contrariwise directed HVOF process gas flow when leaving the substrate surface during a pass.

Despite its insignificant results, FDV was suspected to affect in particular DE and was hence varied in a different range (2.3-2.9 rpm) in the subsequent fractional factorial 2^{5-1} design (Table 3 and 4). The KL range was adjusted to 8-10 L/h for two reasons: Firstly, the high kerosene level was associated with better MH, less RRa, less Po and better DE, and secondly, three experiments run at the low kerosene level 7 L/h produced so thin coatings which made a measurement of microhardness impossible. As a result, all eight main effects and the overall mean (intercept) in the model for microhardness (LM MH) could be estimated. However, with the loss of three degrees of freedom, no sample variance, and consequently no *p*-values could be calculated (NA in LM MH model).

Low kerosene levels of ≤7 L/h only lead to an inadequate heat transfer from the HVOF flame to the fine 75Cr_3C_2-25(Ni20Cr) particles. As a result, an insufficient particle melting occurs, leading to a particle rebounding while impacting on the substrate surface as well as to a poor particle embedding in the coating morphology and poor cohesion strength of the individual coating lamellae. Figure 4 shows the highly porous, strongly defective coating morphology containing many unmelted Cr_3C_2 particles which is not applicable.

As large stand-off distances were associated with less roughness, but also lower deposition efficiency, SOD will be analyzed further in an extended range from 100 to 160 mm. The negative effect of HL on RRa led to the decision to adjust the HL range to 60-100 L/min; OL was kept at 800-900 L/min.

3.3 Fractional Factorial Design 2^{5-1} (Modelling)

In a 2^{5-1} design, the five main effects and all ten possible two-way interactions are not confounded with each other and can be estimated when ignoring all interactions of a

Table 3 Fractional factorial 2^{5-1} design with three additional center runs, and corresponding results

No.	Microhardness (MH), HV 0.1	Roughness Ra (RRa), µm	Porosity (Po), %	Deposition efficiency (DE), %	Kerosene level (KL)	Hydrogen level (HL)	Oxygen level (OL)	Stand-off distance (SOD)	Feeder disc velocity (FDV)
1	857	3.49	0.59	37.41	−1	−1	−1	−1	+1
2	818	8.97	1.15	66.78	+1	−1	−1	−1	−1
3	801	3.63	0.72	32.67	−1	+1	−1	−1	−1
4	771	6.06	1.53	51.69	+1	+1	−1	−1	+1
5	720	4.44	0.77	33.90	−1	−1	+1	−1	−1
6	827	10.15	0.69	43.47	+1	−1	+1	−1	+1
7	703	4.87	0.94	31.51	−1	+1	+1	−1	+1
8	952	13.10	0.99	50.34	+1	+1	+1	−1	−1
9	467	3.48	1.15	22.40	−1	−1	−1	+1	−1
10	682	2.19	0.86	31.67	+1	−1	−1	+1	+1
11	664	3.33	1.35	24.53	−1	+1	−1	+1	+1
12	681	1.99	0.64	37.40	+1	+1	−1	+1	−1
13	509	5.00	1.96	21.58	−1	−1	+1	+1	+1
14	748	2.95	0.50	32.88	+1	−1	+1	+1	−1
15	582	4.19	1.40	25.27	−1	+1	+1	+1	−1
16	717	2.65	0.57	31.51	+1	+1	+1	+1	+1
17	827	3.03	0.48	38.50	0	0	0	0	0
18	809	3.19	0.74	39.24	0	0	0	0	0
19	771	2.93	0.65	41.46	0	0	0	0	0

Table 4 Effect estimates and *p*-values ($\alpha = 0.1$) for the fractional factorial 2^{5-1} design

	Microhardness (MH), HV 0.1		Roughness Ra (RRa), µm		Porosity (Po), %		Deposition efficiency (DE), %	
	Estimate	*p*-Value	Estimate	*p*-Value	Estimate	*p*-Value	Estimate	*p*-Value
Intercept	731.9	0.000	4.72	0.002	0.93	0.001	36.54	0.000
Kerosene level (KL)	55.8	0.069	0.98	0.121	−0.12	0.260	7.28	0.004
Hydrogen level (HL)	15.2	0.504	−0.05	0.915	0.03	0.760	−0.32	0.750
Oxygen level (OL)	1.1	0.961	0.89	0.146	−0.01	0.912	−2.13	0.105
Stand-off dist. (SOD)	−87.4	0.022	−1.81	0.029	0.07	0.510	−7.53	0.004
Feeder disc velocity (FDV)	−2.4	0.911	−0.31	0.541	0.07	0.467	−1.77	0.152
KL * HL (interaction)	−9.4	0.670	−0.00	0.993	0.04	0.703	−0.16	0.874
KL * OL (interaction)	35.4	0.175	0.32	0.536	−0.17	0.152	−1.54	0.195
KL * SOD (interaction)	19.9	0.394	−1.75	0.031	−0.29	0.046	−2.32	0.087
KL * FDV (interaction)	−22.8	0.338	−0.43	0.413	−0.03	0.780	−1.87	0.137
HL * OL (interaction)	3.6	0.870	0.34	0.513	−0.03	0.741	1.17	0.295
HL * SOD (interaction)	14.6	0.520	−0.13	0.795	−0.09	0.367	1.60	0.183
HL * FDV (interaction)	−17.7	0.443	−0.44	0.408	0.01	0.943	0.96	0.375
OL * SOD (interaction)	6.7	0.7608	−0.41	0.4310	0.06	0.517	1.54	0.196
OL * FDV (interaction)	−28.3	0.2529	0.06	0.9005	−0.01	0.912	−0.02	0.982
SOD * FDV (interaction)	14.2	0.5303	0.38	0.4618	0.06	0.556	0.68	0.513

higher order than two. Additional experiments in the design center provide three degrees of freedom for the estimation of the overall variance. In contrast to the previous screening design, the significance level was now chosen as $\alpha = 0.1$ in order to make significance statements more reliable. Estimates and *p*-values captured in Table 4 demonstrate the high importance of KL and SOD regarding not only main effects, but in particular their interaction effect, which is significant with respect to all responses except MH. For MH, however, both main effects are active as demonstrated in Fig. 5(a) for KL and Fig. 5(b) for SOD. While KL has a positive effect on MH, the effect of SOD is negative, so in terms of microhardness, high kerosene levels and short stand-off distances are to be preferred. According to Table 4, the surface roughness RRa is largely determined by KL and SOD, which also show a strong interaction expressed by the non-parallel lines in Fig. 6(a).

While overall, high kerosene levels produce comparably rough surfaces, this is true especially for short stand-off distances (SOD). The best, i.e. lowest, RRa results (1.99-2.95 µm), however, are accomplished with a combination of large SOD and high KL. All three center runs provide very good results (2.93-3.19 µm) as well. The porosity of the coating is largely determined by the significant interaction ($p = 0.046$) of KL and SOD (Fig. 6b). While KL has a positive effect on Po at the low level of SOD, the influence is even stronger and negative at large stand-off distances. All experiments run at the combination KL 10 L/h/SOD 160 mm produce coatings with Po values between 0.5 and 0.86%. The three center runs also provide low porosities between 0.48 and 0.74%.

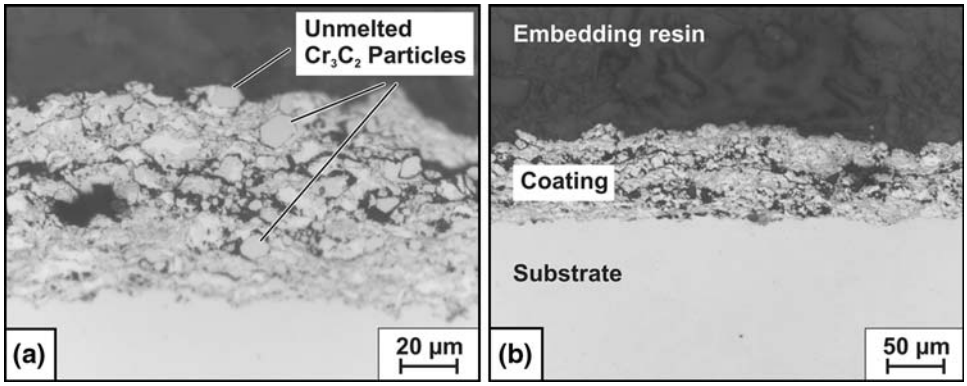

Fig. 4 Poor particle embedding in the coating morphology and poor cohesion strength of the individual coating lamellae occurring while spraying with low kerosene levels ≤7 L/h

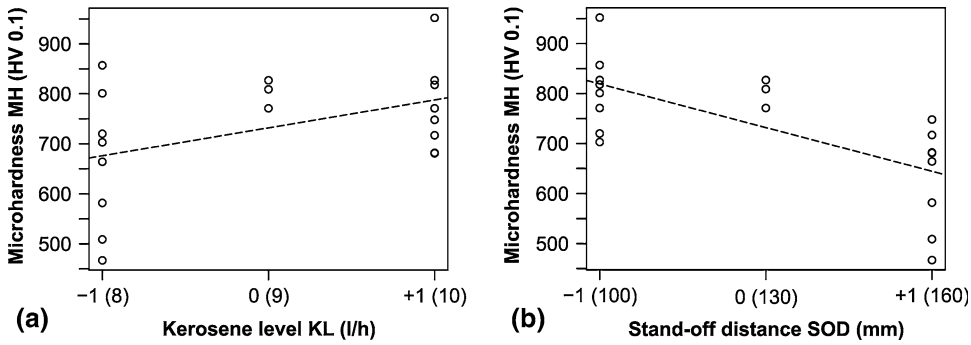

Fig. 5 Main effects of (a) KL and (b) SOD with respect to MH

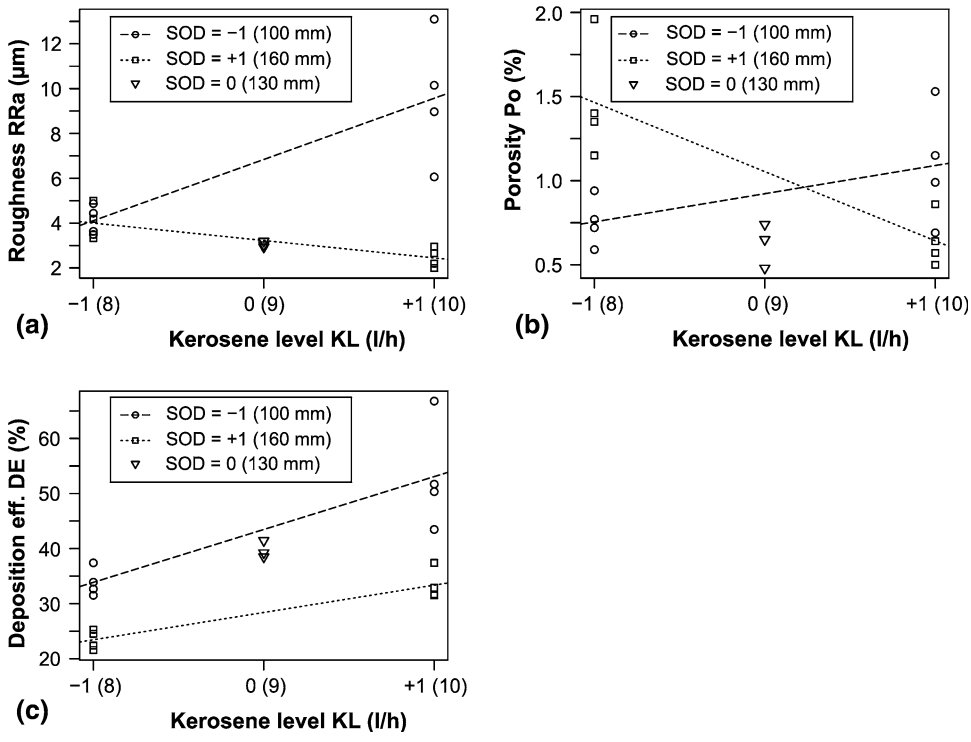

Fig. 6 Interaction effects of KL and SOD with respect to (a) RRa, (b) Po and (c) DE

In terms of the deposition efficiency, again KL and SOD are the most important factors with a significant interaction effect ($p = 0.087$). The by far highest deposition efficiencies (43.47-66.78%) are achieved with the combination of short stand-off distance and high kerosene level (Fig. 6c). OL, HL and FDV are not significant for any response variable, but for OL some p-values between 0.1 and 0.2 are observed. Figure 5(a) and (b), showing the main effects of KL and SOD on microhardness, suggest to take into consideration quadratic effects, which is done in a more complex model based on a Central Composite design for the factors KL, OL and SOD.

3.4 Central Composite Design (Optimization)

In addition to the experiments of a Fractional-Factorial design, which are the corner points of a hypercube, a Central Composite design includes several center points and two axial points for every factor considered in the design. For each factor they are at a distance d to either side of the center, with all other factors held at the level 0 (Fig. 7).

While the distance d is usually chosen in a way to achieve orthogonality or rotatability of the design (Ref 26), here it is chosen as $d = 2$ for the practical reason that with the CJS-HVOF device being used, KL can only be adjusted in steps of 1 L/h. Table 1 summarizes the level settings of the factors KL, OL and SOD in the Central Composite design and Table 5 shows the corresponding results. With five levels for each process parameter, all main and quadratic effects and all two-way interactions can be estimated.

While it is possible to simply use all effect estimates to model a response surface, it is common practice to select only those effects that contribute to optimizing a criterion of model fit, such as the AIC, which weighs out the residual sum of squares and the number of effects used in the model. Using the R function "stepAIC" (Ref 27), for each response the best fit is determined, allowing the algorithm to choose from all of the above linear and quadratic as well as interaction effects. Starting with a model including only one constant (intercept), effects are added or dropped stepwise until no further improvement, i.e. reduction of the AIC criterion is possible. The resulting models are:

(LM MH) MH [HV 0.1]: $Y_{MH} = 784.57 + 66.77 \cdot KL + 30.90 \cdot OL^2 - 60.51 \cdot OL + 48.07 \cdot SOD^2 - 46.86 \cdot SOD + \varepsilon$(Residual standard error = 95.73, adjusted $R^2 = 0.54$)

(LM DE) DE [%]: $Y_{DE} = 55.01 - 4.11 \cdot KL^2 + 5.54 \cdot KL - 7.58 \cdot OL - 4.85 \cdot SOD - 2.99 \cdot (OL \cdot KL) + \varepsilon$(Residual standard error = 6.64, adjusted $R^2 = 0.73$)

(LM RRa) RRa [μm]: $Y_{RRa} = 2.06 + 0.95 \cdot SOD^2 - 1.06 \cdot SOD + \varepsilon$(Residual standard error = 1.40, adjusted $R^2 = 0.53$)

(LM Po) Po [%]: Cannot be modeled

Similar to the AIC criterion, the adjusted R^2 is a measure of model fit, which relates the variance explained by the independent variables to the overall variance, adjusting for the number of effects used in the model. Unlike the simple R^2, which lies between 0 and 1, the adjusted R^2 can even fall below 0, due to the corrections made for the number of considered effects.

For Po no effect could establish an improvement compared to the very basic model including only an intercept. This is in line with difficulties experienced in previous designs for Po, and it seems as if Po cannot be properly modelled with the considered process variables. It is therefore dropped from further analysis.

While residual standard errors in models (LM MH) and (LM DE) are considerably small related to the overall mean (intercept) that in (LM RRa) is large, accounting for almost 3/4 of the mean, and results in large prediction intervals (compare Fig. 9 in the section about "Verification experiments") it is, however, largely induced by one single observation made at SOD = 100 mm (−2), where RRa = 10.71 μm, while the mean of the remaining 17 observations is 2.44 μm and the second largest observation is 4.11 μm. Dropping this highly influential point would result in a completely different model (using only KL^2 and KL) with an overall mean (intercept) of 2.12 and residual standard error of 0.34. Results from the Fractional-Factorial design have shown that the observed high measurement is typical for runs at SOD = 100 mm (Fig. 6a and Table 3), supporting the decision to use model (LM RRa) despite the large residual standard error.

In order to find an optimum overall setting of these most influencing process factors, response surface methodology is subsequently applied under utilization of Derringer's desirability function (Ref 21) and the desirability index. Desirability functions allow to transfer each of the response variables into the interval [0, 1] in order to make them comparable and to combine them into one common measure—the desirability index, e.g. the geometric mean. The simultaneous consideration of all response variables

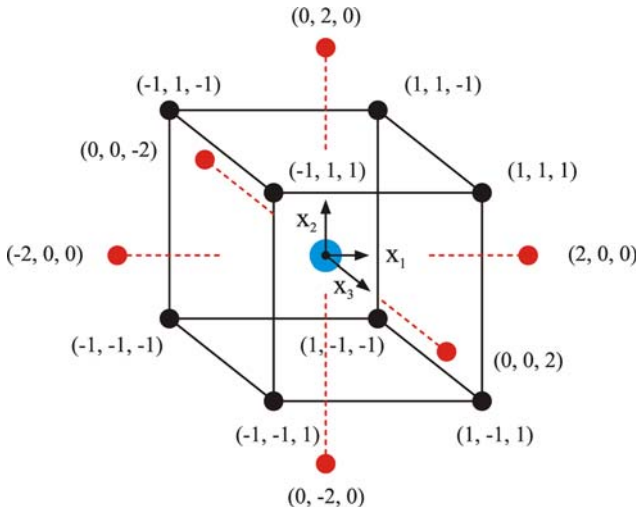

Fig. 7 Central Composite design with six axial points at a distance 2 from the design center

Table 5 Central Composite design and corresponding results

No.	Microhardness (MH), HV 0.1	Roughness Ra (RRa), µm	Porosity (Po), %	Deposition efficiency (DE), %	Kerosene level (KL)	Oxygen level (OL)	Stand-off distance (SOD)
1	827	2.21	1.22	59	−1	−1	−1
2	794	2.75	1.73	50	−1	−1	1
3	786	2.53	4.68	51	−1	1	−1
4	592	3.18	2.14	37	−1	1	1
5	1052	1.98	1.96	69	1	−1	−1
6	877	2.02	1.73	59	1	−1	1
7	783	2.87	1.35	53	1	1	−1
8	921	1.79	1.17	30	1	1	1
9	648	4.11	1.99	20	−2	0	0
10	865	2.91	1.89	57	2	0	0
11	1068	2.04	3.19	66	0	−2	0
12	818	2.00	1.47	39	0	2	0
13	1133	10.71	1.87	62	0	0	−2
14	890	2.16	2.70	51	0	0	2
15	712	2.72	0.90	45	0	0	0
16	926	1.88	1.36	58	0	0	0
17	946	2.17	1.69	60	0	0	0
18	750	2.14	2.15	58	0	0	0

in one common index, which is to be optimized, allows to make necessary compromises between competing responses (Fig. 6a, c). While high kerosene levels at short stand-off distances produce the best DE results, they also lead to the most undesirable RRa observations.

4. Multi-Criteria Optimization of HVOF Spray Experiments

The idea of multi-criteria optimization is to find a combination of the independent variables that optimizes ideally all responses at once, or at least constitutes the best possible compromise.

4.1 Overlayed Contours

If the number of responses is small, as is the case here, overlayed contour plots can assist in finding an optimum overall setting of the independent variables. Figure 8 shows the contours for MH, DE and RRa at KL levels 1 (Fig. 8a) and 2 (Fig. 8b). It is quite obvious that MH improves while moving away in circles from (OL = 1/SOD = 0.5), DE gets better as OL decreases, and RRa takes its lowest value in the valley where SOD = 0.56.

Comparing the plots in Fig. 8(a) and (b) indicates a small advantage of KL = 2 over KL = 1, as e.g. in (OL = −2/SOD = 0.56) the prediction for the most important response MH clearly exceeds 1100 with KL = 2, while with KL = 1 it stays just below this mark. However, as kerosene settings of 12 L/h (KL = 2) and more lead to severe powder caking formation in the powder injectors and the acceleration nozzle, 11 L/h (KL = 1) is a preferred setting—remembering that KL can only be varied in steps of 1 L/h (compare section ''Central Composite Design (Optimization)'').

A disadvantage of contour plots of the original responses is that they do not provide an answer to the question of how a setting, which gives rather good results for all responses (like the one just discussed), compares with a setting that produces a poor result for one response, but an excellent one for another (such as KL = 1/OL = −2/SOD = −2). In order to be able to make such comparisons all responses must be combined into one single measure.

4.2 Desirabilities

Before several response variables can be combined, they must be measured on a common scale. One very practical method to achieve this is to apply Derringer's desirability function (Eq 3, exemplarily for maximization problems), where the desirability of a response Y takes on the value 0 when Y falls below a lower specification limit (LSL), and the value 1 as Y exceeds the upper specification limit (USL) (Ref 21), which in the case of maximization problems (e.g. MH and DE) characterizes an optimal value. Accordingly, LSL and USL have the opposite meaning for minimization problems (e.g. RRa and Po).

$$d(Y) = \begin{cases} 0 & \text{if} \quad Y<\text{LSL} \\ \left(\frac{Y-\text{LSL}}{\text{USL}-\text{LSL}}\right)^s & \text{if} \quad \text{LSL} \le Y \le \text{USL} \\ 1 & \text{if} \quad Y>\text{USL} \end{cases} \qquad \text{(Eq 3)}$$

Values in between the limits are assigned desirabilities according to Eq 3, where the transformation is linear if $s = 1$. Lower and upper specification limits must be specified by a process engineer who can decide which values of a response are desired. The desirability transformation is applied to the predicted responses which can be made using the models (LM MH, LM DE, LM RRa). Once all new responses have the same desirability scale, they can be combined into one desirability index, which is commonly calculated as the weighted geometric mean (Eq 4).

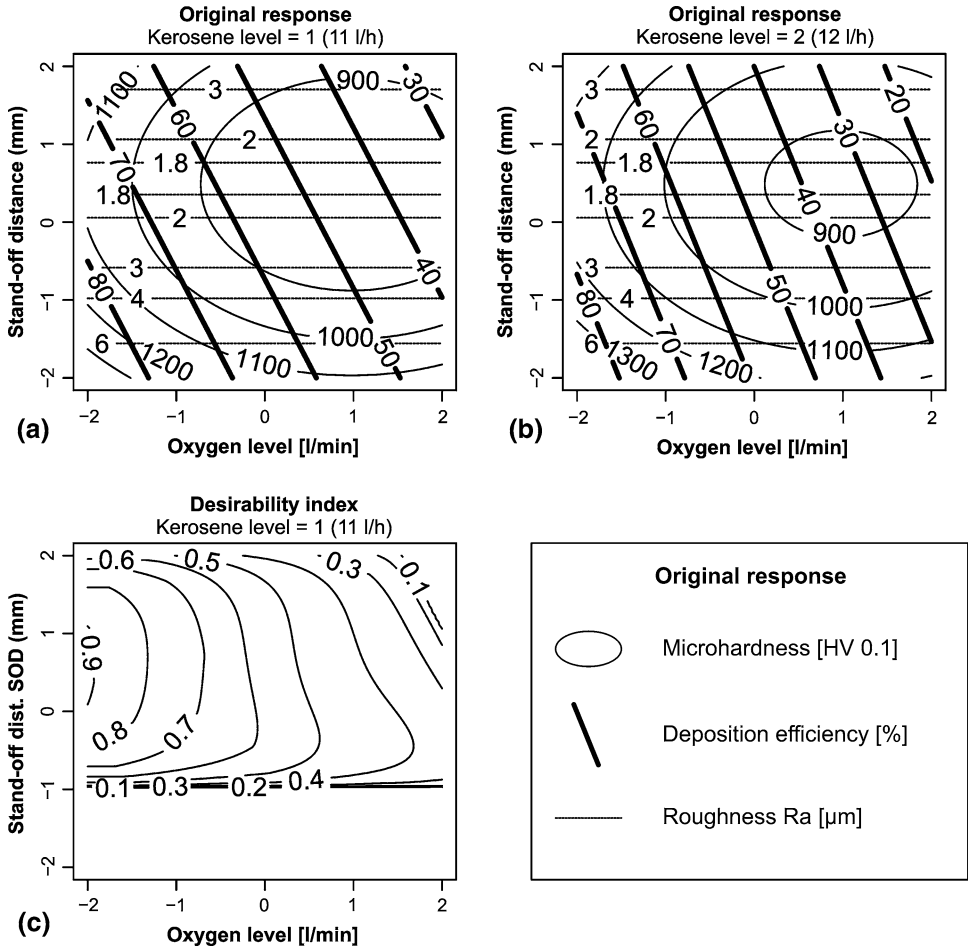

Fig. 8 Contour plots of the original responses (a, b) and the desirability index (c) using the weighted geometric mean with weights (MH = 0.4/DE = 0.35/RRa = 0.25)

Table 6 Parameters for desirability transformations ($s = 1$ in all cases)

	Microhardness, HV 0.1		Deposition efficiency, %		Roughness Ra, µm	
	MH (max)	*d* (MH)	DE (max)	*d* (DE)	RRa (min)	*d* (RRa)
Lower specification limit (LSL)	700	0	30	0	1	0
Upper specification limit (USL)	1100	1	60	1	4	1

$$D_{GM} = \prod_{i=1}^{p} (d_i(Y_i))^{w_i} \qquad \text{(Eq 4)}$$

with weights $w_i > 0$ and $\sum_{i=1}^{p} w_i = 1$ for p quality criteria. After transforming the original responses into desirabilities according to Table 6 using the R-package "desiRe" (Ref 28) contours of the desirability index with weights (MH = 0.4/DE = 0.35/RRa = 0.25) shown in Fig. 8(c) enable to make comparisons between different settings very easily.

For example, the two settings compared in the section "Overlayed contours" correspond to desirabilities of 0.92 (KL = 1/OL = −2/SOD = 0.56) and 0 (KL = 1/OL = −2/SOD = −2). The second setting is completely undesirable because of unacceptable roughness predictions (≥4 µm) for SOD < −1. An optimization of the desirability index in R yields the optimum setting (KL = 1.42/OL = −2.2/SOD = 0.56) with a desirability of 0.93. The imbalanced weighting is chosen in order to ensure an optimum with particularly good MH, which is the most important characteristic for typical applications.

4.3 Verification Experiments

The results of four verification experiments in the vicinity of the theoretical optimum are compared with their predicted values in Table 7.

Table 7 Predicted and experimentally determined coating properties at optimized spray parameters as well as the relative deviance between these values

No.	KL, L/h	OL, L/min	SOD, mm	Deposition efficiency (DE), %			Layer thickness , µm	Microhardness (MH), HV 0.1			Po, %	Roughness Ra (RRa), µm		
				Pred.	Exp.	Dev., %		Pred.	Exp.	Dev., %	Exp.	Pred.	Exp.	Dev., %
(a)	1	−2	0.56	74.85	74.41	0.59	185	1084.15	1129.50	4.18	1.60	1.76	1.83	4.11
(b)	1	−2	0.56	74.85	76.10	1.67	150	1084.15	1017.62	6.14	1.93	1.76	1.97	11.72
(c)	1	−2	0.56	74.85	61.57	17.75	155	1084.15	864.57	20.25	1.58	1.76	1.82	3.54
(d)	2	−2	0.56	74.04	68.83	7.03	152	1150.85	1127.47	2.03	1.37	1.76	2.28	29.79

Pred. = predicted value, Exp. = experimental value, Dev. = relative deviance of the predicted vs. experimentally determined value

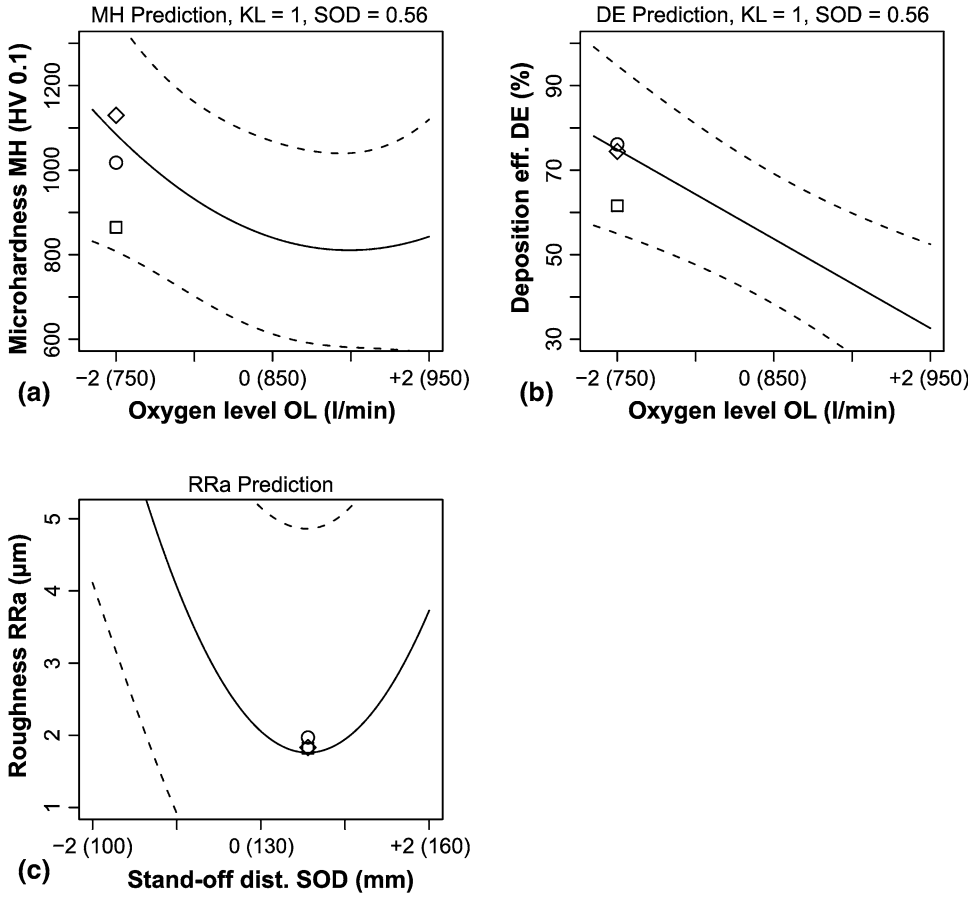

Fig. 9 Prediction line and 95% prediction interval lines (dashed) for MH, DE and RRa based on the models LM MH, LM DE and LM RRa fit from the data of the Central Composite design (Table 5). Three verification experiments at (KL = 1, OL = −2, SOD = 0.56) near the theoretically determined optimum are included and lie within the prediction intervals

Because KL can only be varied in steps of 1 L/h according to the adjustability of the HVOF device, it is not possible to conduct experiments at KL = 1.42 L/h. Therefore, experiments at KL = 1 (11 L/h) and KL = 2 (12 L/h) have been conducted alternatively. Due to a significant increase of undesired powder caking formations in the powder injectors and the acceleration nozzle at high kerosene levels, KL = 1 is strongly preferred over KL = 2. For this reason only one experiment (d) has been carried out at KL = 2, contrasting three runs (experiments a-c in Table 7) with the combination (KL = 1/OL = −2/SOD = 0.56). Despite the theoretical optimum of OL at −2.2 (740 L/min) the setting −2 has been used in order to stay in the region of experimentation.

According to the results in Table 7, spraying with both parameter settings KL = 1 (11 L/h) and KL = 2 (12 L/h) along with constant OL = −2 (750 L/min) and SOD = 0.56 (138 mm) leads to exceptional coating properties with high hardness, low roughness and low porosity at a high deposition efficiency. However, although best coating

properties are obtained here, at KL = 1 a moderate but not negligible, and at KL = 2 a severe formation of powder caking occur inside the acceleration nozzle and the powder injectors.

The comparison of predicted and experimentally determined coating properties and their relative deviance clearly indicates that the models generally provide a very good approximation of the coating properties when using the optimized spray parameters. The results of three verification experiments with this setting are captured in Fig. 9, showing the prediction lines along with their corresponding 95% prediction intervals for MH (Fig. 9a), DE (Fig. 9b) and RRa (Fig. 9c). The prediction lines and intervals are calculated from the models LM MH, LM DE and LM RRa, which were fitted based on the 18 data points from the Central Composite design in Table 5. The results of the three verification experiments near the theoretical optimum are within the prediction limits and account for desirability indexes of 0.93 (◇), 0.83 (○) and 0.65 (□). Here, even the prediction with desirability index 0.65 features acceptable MH (865 HV 0.1), very good RRa (1.82 μm), and DE (61.6%), which corresponds to desirability 1 for DE. DE for the other two experiments is exceptional (76.1 and 74.4%). The latter of these two experiments (the one with a DE of 74.4%) also accomplishes exceptional MH (1130 HV 0.1) with corresponding desirability 1 for MH.

The comparison of the first two experiments (experiments a and b in Table 7) presents only small differences in MH and DE values along with very small relative deviances. For the second experiment the relative deviance for RRa is somewhat higher (11.72 μm). In contrast, the third experiment (experiment c in Table 7) features the highest relative deviation in the coating properties in MH (17.75 HV 0.1) and DE (20.25%) but the lowest value concerning RRa (3.54 μm). Experiment d in Table 7 also shows a good approximation for DE (7.03%) and MH (2.03 HV 0.1) but a large relative deviance for RRa (29.79 μm).

4.4 Coating Properties at Optimized Spray Parameter Settings

Finally, the as-sprayed coating morphology sprayed with spray parameters KL = 1 (11 L/h), OL = −2 (750 L/min), SOD = 0.56 (138 mm) optimized using statistical design of experiments through three design stages (Plackett-Burman, Fractional-Factorial and Central Composite designs) were microscopically analyzed. Figure 10(a) and (b) reveal a complex, multi-phase structure composed of finely dispersed chromium carbides and nickel chromium binder phases which are created by a flattening of molten particles upon impact. Thermal spraying of fine 75Cr_3C_2-25(Ni20Cr) enables the deposition of cermet

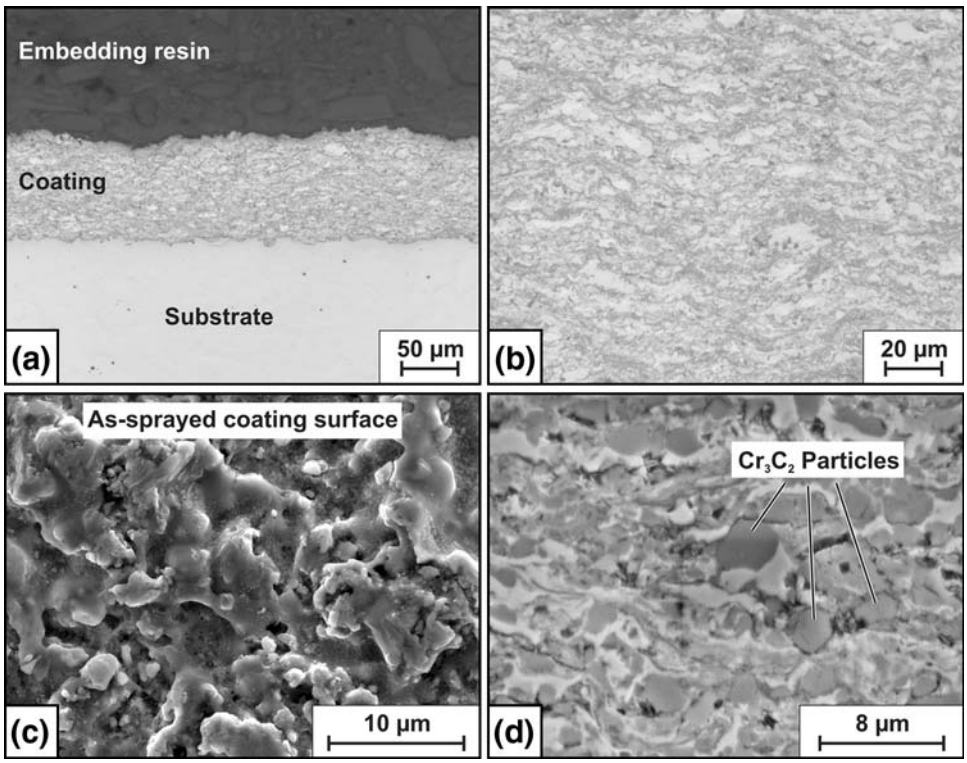

Fig. 10 (a, b) Cross-sectional images of the fine structured coating morphology and the interface between coating and substrate material taken by light microscope, (c) SEM image of the as-sprayed coating surface and (d) cross-sectional image of the coating morphology taken by SEM

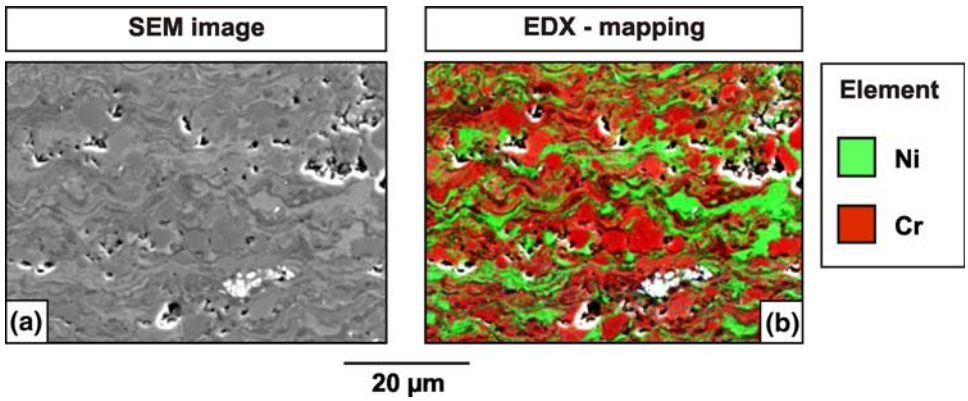

Fig. 11 EDX mapping showing the phases elements in the coating morphology

coatings with an extremely dense, fine structured and homogenous morphology with porosities <1%. Only small-sized micro-pores and thin voids on a submicron and nanosized level are detectable in regions of imperfect contact between the phases or lamellae. These results can be attributed to the high velocity of the fine particles (816 ± 11 m/s) and the moderate particle temperature (2150 ± 5 °C) which both have been measured in-flight at optimized spray parameters. Figure 10 also shows SEM images of the as-sprayed coating surface (Fig. 10d) and the coating morphology (Fig. 10d) at a higher magnification level. Both images clearly demonstrate the extremely fine structure which also provides a superior surface quality. It can also be seen that the fine-scaled, irregular chromium carbide particle structure is preserved in the coating morphology, well embedded in a homogenously molten nickel chromium binder phase (Fig. 10d). EDX analyses in Fig. 11 confirmed that the dark phases in the SEM picture primary consist of chromium carbide (labeled in dark gray), whereas the lighter phases are composed of a nickel chromium (labeled in light gray) alloy.

Figure 10(a) also demonstrates an excellent interface bonding between the coating and the roughened C45-steel surface. It seems as if a substrate preparation using fine-grained alumina as blasting medium (106-150 µm) leads to an appropriate roughness profile for the subsequent coating operation in terms of the coating adhesion. Adhesion tests showed an average adhesive strength of 80.4 ± 5.54 N/mm^2.

Figure 12 illustrates the fracture surface of four test samples (each with coated punch and counter punch) after the adhesion test. The samples show a primary rupture of the epoxy resin adhesive from the steel substrate surface, indicating an even higher adhesive strength than measured value. Besides, a minor part of cohesive breakages in the coating morphology occur as well, demonstrated by coating residues in Fig. 12.

The as-sprayed coatings also feature a smooth surface with roughness values Ra < 2 µm. As reported in literature, the application of fine powders leads to an increase in

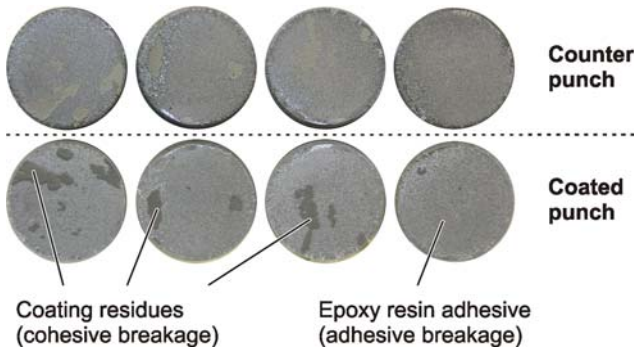

Fig. 12 Fracture surfaces of the samples after the adhesion test

layer homogeneity attributed to a better fusibility of finescaled materials and a finer dispersed phase distribution in the coating structure (Ref 29). This is correlated with a decrease in surface roughness (Ref 30). The splat densification level and the corresponding roughness of the as-sprayed coatings are mainly affected by the particle velocity and the molten state of the sprayed particles. A high velocity of fine particles provided by the HVOF process gas flow, in combination with a better and more homogenous molten state when using finescaled $75Cr_3C_2$-25(Ni20Cr) powders, help to deform or flatten the particle as splat upon impact.

The fine structured $75Cr_3C_2$-25(Ni20Cr) coatings sprayed with optimized parameters [KL = 1 (11 L/h), OL = −2 (750 L/min) and SOD = 0.56 (138 mm)] show a wear coefficient of 4.69 × 10^{-7} g/Nm measured by Pin-on-Disc test and a wear coefficient of 1.68 × 10^{-8} g/Nm determined by Taber Abraser. Compared to the wear coefficient of the uncoated steel sample by Taber Abraser (1.02 × 10^{-7} g/Nm), an up to six times higher wear resistance can be provided by the one with a fine structured surface coating. Figure 13 gives a comparison of the friction coefficient development of the grinded (Fig. 13a) and the as-sprayed coating surface (Fig. 13b). Figure 13(a) shows a first initial peak, suggesting the static friction

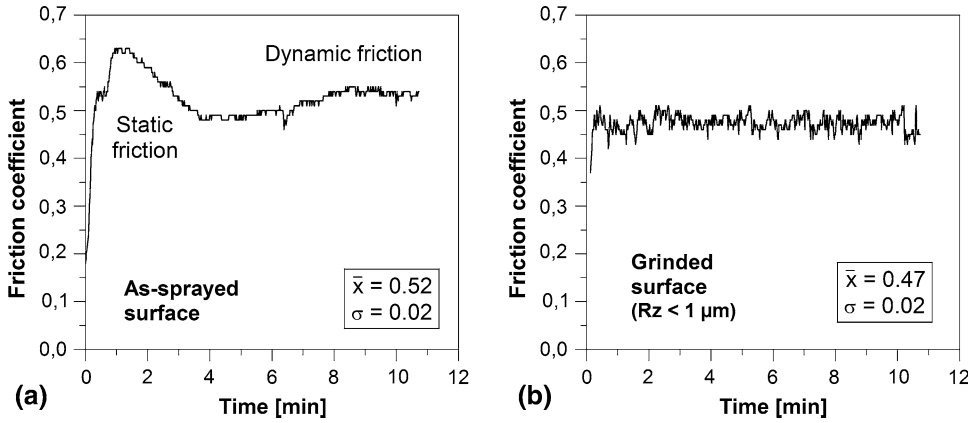

Fig. 13 Friction coefficient development of the (a) as-sprayed and (b) grinded $75Cr_3C_2$-25(Ni20Cr) coating surface using an alumina ball

coefficient and indicating the characteristic running-in behavior of the tribological system consisting of the alumina ball and the $75Cr_3C_2$-25(Ni20Cr) coating, which is significantly more distinctive with the as-sprayed surface as the grinded one. Whereas for the as-sprayed surface a nearly constant friction coefficient of 0.52 ± 0.02 (the dynamic friction coefficient) is achieved after a period of approximately 4 min, the as-sprayed coating surface shows a nearly continuous and stable friction coefficient of 0.47 ± 0.02 over the measuring time.

5. Conclusion and Outlook

Statistical design of experiments (DOE) has been successfully employed to identify the most relevant factors influencing the HVOF spraying of fine $75Cr_3C_2$-25(Ni20Cr) powders ($-8+2$ µm) and to find an optimum setting of these factors to produce coatings with improved morphological and mechanical properties. The kerosene level, the oxygen level, the stand-off distance as well as the two-way kerosene/stand-off distance interaction could be identified as the most significant influencing factors with respect to the deposition efficiency, roughness and microhardness. The coating characteristic porosity could not be properly modeled with the independent variables under study. Using response surface methods, overlayed contour plots of the original responses, and the concept of desirability functions as well as the desirability index, optimum spray settings could be identified. Next to a stand-off-distance of 138 mm, a theoretical optimum for the oxygen level was obtained at 740 L/min. In four verification experiments the setting 750 L/min was used in order to stay inside the region of experimentation. Powder caking inside the acceleration nozzle and the powder injectors, attributed to a rapid overheating of the fine spray particles at high kerosene levels particularly in combination with insufficient carrier gas levels (higher than 9 L/min or lower than 11 L/min) could be revealed as the most problematic effects in the HVOF process. The optimum kerosene level was identified to lie between 11 and 12 L/h. However, a kerosene level of 11 L/h is preferred over 12 L/h to reduce the risk of the mentioned powder caking formation. Further problems are represented by the formation of horizontal cracks and powder agglomerations in the HVOF process which embed in the coating microstructure. To avoid these effects, stand-off distances >100 mm should be favored.

Verification experiments yielded mostly excellent results in close proximity to the predicted values. The deposited fine structured coatings showed an extremely dense and finely dispersed coating structure (porosity $<$ 2%), a high surface quality (Ra $<$ 2 µm) and a high adhesive strength. These coatings show a high potential to be used as wear resistant coatings for large tools without any post treatment or surface finish.

A further challenge is the examination of the oxygen level in an extended range below 750 L/min and to find a promising factor setting with lower kerosene level <11 L/h, which causes much less powder caking. It can be concluded that the employment of statistical design of experiments represented an effective method to find optimized spray parameters to produce coatings with superior properties.

Acknowledgments

The authors gratefully acknowledge the financial support of the DFG (German Science Foundation) within the Collaborative Research Centres SFB 475 and SFB 708, and the Transregional Collaborative Research Centre SFB TRR 30.

References

1. J. Morimoto, Y. Sasaki, S. Fukuhara, N. Abe, and M. Tukamoto, Surface Modification of Cr_3C_2–NiCr Cermet Coatings by Direct Diode Laser, *Vacuum*, 2006, **80**(11-12), p 1400-1405
2. R. Nieminen, P. Vuoristo, K. Niemi, T. Mantyla, and G. Barbezat, Rolling Contact Fatigue Failure Mechanisms in Plasma and HVOF Sprayed WC-Co Coatings, *Wear*, 1997, **212**(1), p 66-77
3. K. Bobzin, F. Ernst, J. Zwick, and G. Matthäus, Analysis of In-Flight Particle Properties of Thermal Sprayed Ultrafine Powders, *Mater. Sci. Eng. Technol.*, 2007, **38**(2), p 149-154

4. S. Zimmermann, H. Keller, and G. Schwier, Improved Coating Properties by Optimized Carbide Powders for Modern HVOF Systems, *6th HVOF Spraying Colloquium*, Nov 27-28 (Germany), GTS e.V., 2003, p 31-38
5. Y. Qiao, T.E. Fischer, and A. Dent, The Effects of Fuel Chemistry and Feedstock Powder Structure on the Mechanical and Tribological Properties of HVOF Thermal-Sprayed WC-Co Coatings with Very Fine Structures, *Surf. Coat. Technol.*, 2003, **172**(1), p 24-41
6. J.M. Guilemany, S. Dosta, J. Nin, and J.R. Miguel, Study of the Properties of WC-Co Nanostructured Coatings Sprayed by High-Velocity Oxyfuel, *J. Therm. Spray Technol.*, 2005, **14**(3), p 405-413
7. K. Bobzin, F. Ernst, J. Zwick, and G. Matthaeus, Analyse von Partikeleigenschaften beim Thermischen Spritzen von Mikropulvern (Analysis of the Particle Properties in Thermal Spraying of Micronpowders), *Mat.-wiss. u. Werkstofftech.*, 2007, **38**(2), p 149-154 (in German)
8. S. Matthews, M. Hyland, and B. James, Microhardness Variation in Relation to Carbide Development in Heat Treated Cr_3C_2–NiCr Thermal Spray Coatings, *Acta Mater.*, 2003, **51**(14), p 4267-4277
9. W. Tillmann, E. Vogli, I. Baumann, G. Matthaeus, and T. Ostrowski, Influence of the HVOF Gas Composition on the Thermal Spraying of WC-Co Submicron Powders (−8 +1 μm) to Produce Superfine Structured Cermet Coatings, *J. Therm. Spray Technol.*, 2008, **17**(5-6), p 924-932
10. D. Toma, W. Brandl, and G. Marginean, Wear and Corrosion Behaviour of Thermally Sprayed Cermet Coatings, *Surf. Coat. Technol.*, 2001, **138**, p 149-158
11. J.A. Picas, A. Forna, A. Igartuab, and G. Mendozab, Mechanical and Tribological Properties of High Velocity Oxy-Fuel Thermal Sprayed Nanocrystalline CrC-NiCr Coatings, *Surf. Coat. Technol.*, 2003, **174-175**, p 1095-1100
12. D.C. Crawmer, J.D. Krebsbach, and W.L. Riggs, Coating Development for HVOF Process Using Design of Experiment, *Thermal Spray: International Advances in Coatings Technology*, C.C. Berndt, Ed., ASM International, Materials Park, OH, 1992, p 127-136
13. L. Russo and M. Dorfmann, *Thermal Spraying, Current Status and Future Trends*, A. Ohmori, Ed., Japan High Temperature Society, Osaka, 1995, p 681-686
14. K. Kreye, R. Schwetzke, and S. Zimmermann, High Velocity Oxy-Fuel Flame Spraying-Process and Coating Characteristics, *Thermal Spray: Practical Solutions for Engineering Problems*, C.C. Berndt, Ed., ASM International, Materials Park, OH, 1996, p 451-456
15. J.M. Guilemany and J.A. Calero, *Structural Evaluation Phenomena During High Velocity (HVOF) of the Composite Material Cr_3C_2-NiCr, Surface Modification Technologies XI*, T.S. Sudarshan, et al., Ed., The Institute of Materials, Paris, 1997, p 81-85
16. K. Taoa, X. Zhoua, H. Cuib, and J. Zhanga, Microhardness Variation in Heat-Treated Conventional and Nanostructured NiCrC Coatings Prepared by HVAF Spraying, *Surf. Coat. Technol.*, 2009, **203**(10-11), p 1406-1414
17. G.C. Jia, C.J. Lib, Y.Y. Wang, and W.Y. Lib, Microstructural Characterization and Abrasive Wear Performance of HVOF Sprayed Cr_3C_2-NiCr Coating, *Surf. Coat. Technol.*, 2006, **200**(24), p 6749-6757
18. V.V. Sobolev and J.M. Guilemany, Effect of Oxidation on Droplet Flattening and Splat-Substrate Interaction in Thermal Spraying, *J. Therm. Spray Technol.*, 1999, **8**(4), p 523-530
19. N. Eigen, F. Gärtner, T. Klassen, E. Aust, R. Bormann, and H. Kreye, Microstructures and Properties of Nanostructured Thermal Sprayed Coatings Using High-Energy Milled Cermet Powders, *Surf. Coat. Technol.*, 2005, **195**, p 344-357
20. L. Gil and M.H. Staia, Influence of HVOF Parameters on the Corrosion Resistance of NiWCrBSi Coatings, *Thin Solid Films*, 2002, **420-421**, p 446-454
21. G. Derringer and R. Suich, Simultaneous Optimization of Several Response Variables, *J. Qual. Technol.*, 1980, **12**, p 214-219
22. G. Matthaeus, M. Kostecki, and O. Dau, The Fully Automatic, Computer Controlled C-CJS (Computerised Carbide Jet System) HVOF System with 25 bar Combustion-Chamber Pressure by Thermico, *5th Colloquium on HVOF Flame Spraying, Flame Spraying*, Nov 16-17 (Germany), GTS e.V., 2000, p 147-158
23. R-Development Core Team, R: A Language and Environment for Statistical Computing. R-Foundation for Statistical Computing, Vienna, Austria. ISBN 3-900051-07-0, 2008
24. H. Chena, G. Goua, M. Tub, and Y. Liua, Characteristics of Nano Particles and Their Effect on the Formation of Nanostructures in Air Plasma Spraying WC–17Co Coating, *Surf. Coat. Technol.*, 2009, **203**(13), p 1785-1789
25. T.P. Ryan, *Modern Experimental Design*, Wiley, Hoboken, NJ, 2007
26. D.C. Montgomery, *Statistical Quality Control*, 6th ed., Wiley, New York, 2009
27. W.N. Venables and B.D. Ripley, *Modern Applied Statistics with S*, 4th ed., Springer, New York, 2002
28. H. Trautmann, D. Steuer, O. Mersmann, U. Ligges, and C. Weihs, desiRe: Desirability Functions and Indices in Multicriteria Optimization, R-Package v0.9.6., 2008, http://r-forge.r-project.org/projects/desire
29. O.P. Solonenko, *Advanced Thermophysical Fundamentals of Melt-Droplet-Substrate Interaction and its Application in Thermal Spraying*, Novosibirrsk, Russia, 2003
30. K. Jia and T.E. Fisher, Abrasion Resistance of Nanostructured and Conventional Cemented Carbides, *Wear*, 1996, **1-2**(200), p 206